



Letter

Microwave Land Emissivity Calculations over the Qinghai-Tibetan Plateau Using FY-3B/MWRI Measurements

Ying Wu ^{1,2}, Bo Qian ^{1,2}, Yansong Bao ^{1,2,*}, George P. Petropoulos ^{3,4} , Xulin Liu ⁵ and Lin Li ⁵

¹ Collaborative Innovation Center on Forecast and Evaluation of Meteorological Disasters, Key Laboratory for Aerosol-Cloud-Precipitation of China Meteorological Administration, Nanjing University of Information Science & Technology, Nanjing 210044, China

² School of Atmospheric physics, Nanjing University of Information Science and Technology, Nanjing 210044, China

³ School of Mineral Resources Engineering, Technical University of Crete, Kounoupidiana Campus, Crete 73100, Greece

⁴ Department of Soil & Water Resources, Institute of Industrial & Forage Crops, Hellenic Agricultural Organization (HAO) "Demeter", Larisa 41335, Greece

⁵ Beijing Meteorological Observation Center, Beijing Meteorological Bureau, Beijing 100089, China

* Correspondence: ysbao@nuist.edu.cn

Received: 2 July 2019; Accepted: 10 September 2019; Published: 20 September 2019



Abstract: The Qinghai-Tibetan plateau plays an important role in climate change with its unique characteristics, and the surface emissivity is an important parameter to describe the surface characteristics. It is also very important for the accurate retrieval of surface and atmospheric parameters. Different types of surface features have their own radiation characteristics due to their differences in structure, water content and roughness. In this study, the microwave land surface emissivity (10.65, 18.7, 23.8, 36.5 and 89 GHz) of the Qinghai-Tibetan Plateau was calculated using the simplified microwave radiation transmission equation under clear atmospheric conditions based on Level 1 brightness temperatures from the Microwave Radiation Imager onboard the FY-3B meteorological satellite (FY-3B/MWRI) and the National Centers for Environmental Prediction Final (NCEP-FNL) Global Operational Analysis dataset. Furthermore, according to the IGBP (International Geosphere-Biosphere Program) classified data, the spectrum and spatial distribution characteristics of microwave surface emittance in Qinghai-Tibetan plateau were further analyzed. The results show that almost all 16 types of emissivity from IGBP at dual-polarization (vertical and horizontal) increase with the increase of frequency. The spatial distribution of the retrieving results is in line with the changes of surface cover types on the Qinghai-Tibetan plateau, showing the distribution characteristics of large polarization difference of surface emissivity in the northwest and small polarization difference in the southeast, and diverse vegetation can be clearly seen in the retrieving results. In addition, the emissivity is closely related to the type of land surface. Since the emissivity of vegetation is higher than that of bare soil, the contribution of bare soil increases and the surface emissivity decreases as the density of vegetation decreases. Finally, the source of retrieval error was analyzed. The errors in calculating the surface emissivity might mainly come from spatiotemporal collocation of reanalysis data with satellite measurements, the quality of these auxiliary datasets and cloud and precipitation pixel discrimination scheme. Further quantitative analysis of these errors is required, and even standard procedures may need to be improved as well to improve the accuracy of the calculation.

Keywords: microwave; remote sensing; MWRI (Microwave Radiation Imager); land surface emissivity; Qinghai-Tibetan Plateau

1. Introduction

Land surface emissivity in the microwave region is an important parameter in both the assimilation of microwave radiation data and the retrieval of surface and atmospheric parameters from satellite microwave measurements [1–3]. Accurate values for the land surface emissivity will help to improve the accuracy of global mesoscale weather forecasting [4–7]. However, it is difficult to obtain accurate values for this parameter due to the diversity of land surfaces and this has become one of the main obstacles in the assimilation of terrestrial satellite data and land surface features.

There has been much research on the variation in surface emissivity and spectral characteristics of different types of land surface. Grody et al. proposed a statistical retrieving algorithm for the land surface emissivity in the microwave region of channels relevant to oxygen absorption (50.30, 53.74, 54.96 and 57.97 GHz) using measurements from the Microwave Sounding Unit (MSU) [8]. Jones and Haar used data from the Special Sensor Microwave Imager (SSM/I) to retrieve the microwave land surface emissivity over the central USA [9]. Prigent et al. analyzed SSM/I data for the microwave land surface emissivity over large parts of Europe and extended the SSM/I land surface emissivity calculation to sensors with a non-fixed observing angle [10–12]. Based on the microwave radiative transfer equation, Wilke and McFarland assumed an approximate atmospheric transmittance equal to unity in clear skies and ignored the influence of clouds. With these assumptions, the land surface emissivity is the ratio of the microwave brightness temperature from the satellite and the skin temperature of the land surface [13].

Galantowicz et al. retrieved monthly values of the emissivity and emission depth index using the Advanced Microwave Scanning Radiometer for Earth Observing System (AMSR-E). The fitting errors, stability, self-consistency of the retrieving model and the results of the land surface model provide the basis for the rationality of the subsurface emission hypothesis and the retrieval method [14]. Ringerud et al. developed a semi-empirical model and tested it over the Great Plains region of the southern USA. Their results show a high consistency between the calculated and measured values [15]. Qiu et al. obtained the AMSR-E global instantaneous microwave emissivity under clear conditions [16]. Tian et al. studied the retrieving of the land surface emissivity of different space-borne microwave sensors, and found many differences in the retrieving results from different sensors in different geographical locations over deserts and tropical rainforests [17].

Li et al. reviewed the calculation methods for surface emissivity and physics-based methods and proposed validation techniques for each type of method [18]. Wang et al. deduced a land surface emissivity retrieving algorithm over the Qinghai-Tibetan Plateau through the radiative transfer equation [19]. Gao et al. proposed an improved algorithm to retrieve the land surface emissivity and temperature at the same time on the basis of the spectral index surface emissivity retrieving method without the influence of temperature using rotary enhanced visible and infrared imager data from the Meteosat Second Generation (MSG-2) satellites [20]. Masiello et al. implemented a Kalman filter-based approach for the physical retrieval of surface temperature and emissivity from SEVIRI (Spinning Enhanced Visible and Infrared Imager) infrared observations, and the approach was validated against in situ and satellite observations over land and ocean. The algorithm has been applied to the SEVIRI full disk, and emissivity maps on that global scale have been physically retrieved for the first time [21,22]. With the support of the global precipitation measurement mission, Tian et al. implemented and evaluated various methods of estimating the surface emissivity and its changes in a well-defined common framework [23]. Orimoloye et al. assessed the land surface temperature (LST) and estimated radiation of East London city in Eastern Cape Province of South Africa. They found that rapid urbanization and land cover changes in this area have contributed significantly to increased land surface temperature and surface solar radiation [24]. To improve the spaceborne monitoring over the Qinghai-Tibet Plateau, China, Qu et al. rebuilt a microwave soil moisture product using random forest adopting AMSR-E/AMSR2 Brightness Temperature and soil moisture active passive (SMAP) data [25]. However, to our knowledge, there has been limited research on the microwave land surface emissivity of the Qinghai-Tibetan Plateau using FY-3 microwave Earth Observation (EO) data.

Thus, this study aimed at calculating the land surface emissivity of the Qinghai-Tibetan Plateau based on the simplified microwave radiative transfer equation using data from the Microwave Radiation Imager (MWRI) onboard the FY-3B meteorological EO satellite and the National Centers for Environmental Prediction Final (NCEP-FNL) Global Operational Analysis dataset. The spatial distribution of the surface emissivity of the Qinghai-Tibetan Plateau was obtained based on the International Geosphere-Biosphere Program (IGBP) surface coverage classification dataset.

2. Calculation of Surface Emissivity

2.1. Calculation of Surface Microwave Emissivity

For the non-scattering plane parallel atmosphere, using the Rayleigh-Jeans approximation, the land surface emissivity in the microwave region (ε) can be calculated from the satellite observation values through the atmospheric radiation equation [26]:

$$\varepsilon = \frac{T_B - T_u - T_d \Gamma}{\Gamma(T_s - T_d)}, \quad (1)$$

in which T_B is the bright temperature observation from the satellite and T_s is the surface skin temperature, which can be obtained from NCEP-FNL datasets.

T_u is the upward radiation toward the satellite and can be written as:

$$T_u = \int_{\tau_s}^{\tau_0} B(\tau, T) \exp\left[-\frac{(\tau_s - \tau)}{\mu}\right] d\tau / \mu, \quad (2)$$

T_d is the atmosphere downward radiation and can be written as:

$$T_d = \int_{\tau_0}^{\tau_s} B(\tau, T) \exp\left[-\frac{(\tau - \tau_0)}{\mu}\right] d\tau / \mu, \quad (3)$$

Γ is the transmittance of the atmosphere and can be written as:

$$\Gamma = \exp(-\tau_s / \mu), \quad (4)$$

In the above equations, B is the brightness temperature at each layer with optical depth τ , τ_0 is the optical depth at the top, τ_s is the optical depth at the layer bottom, and $\mu = \cos(\theta)$, where θ is the satellite view angle. The three parameters, i.e., T_u , T_d , and Γ , are computed from the NCEP-FNL temperature and water vapor profiles which serve as input to the microwave absorption model.

Equation (1) suggests that the deviation of parameters such as the brightness temperature, surface skin temperature, and atmosphere temperature and humidity profiles observed by the satellite can lead to retrieval errors [27]. In addition, the radiative transfer results also depend on the cloud coverage (type of clouds, height, and portion of the field of view covered).

2.2. Study Site

The unique topography of Qinghai-Tibetan Plateau in China has an important impact on climate and climate change, and has become a special concern of meteorologists. Relatively limited conventional observation information greatly limits systematic and comprehensive understanding of the region. Considering that satellite observations have good spatial coverage and can provide relatively continuous observations in time and space in this region, this study used satellite observation data to retrieve the microwave land surface emissivity of the Qinghai-Tibetan Plateau.

The Qinghai-Tibetan Plateau occupies a quarter of the total land area of China, covering an area of $>2 \times 10^6$ km² with an average elevation >4 km, about a quarter of the thickness of the troposphere. The northwest of the Qinghai-Tibetan Plateau has a high elevation and is a more complete plateau region, whereas the southeast of the plateau has a lower elevation. The plateau is surrounded by mountains. To the north and south, the mountains trend east-west; the north-south-trending Hengduan Mountains lie to the east and the Himalayas to the west. Due to the dynamic and thermal effects of the plateau, the atmospheric circulation is affected. The unique topography of the Qinghai-Tibetan Plateau makes it play an important role in the circulation of the northern hemisphere. The Qinghai-Tibetan Plateau is very sensitive to changes in the Earth's climate and changes in this region are precursors of climate change in the surrounding areas. The ground surface has a leading role in atmosphere-ground coupling in the climate system and it is therefore important to study the surface parameters of the Qinghai-Tibetan Plateau.

The surface emissivity is an important parameter reflecting the surface thermal radiation characteristics. Its accuracy directly affects the accuracy of the long-wave radiation emitted by the surface, which affects the calculation accuracy of surface net radiation and surface temperature. It is very important in retrieving of surface temperature. Therefore, the difference in surface emissivity determines the long-wave radiation energy distribution under different surface conditions [28,29], which in turn affects the radiation budget and energy balance of the entire surface [30,31].

In view of the advantages of microwave detection on the surface, deep understanding of the characteristics of the land surface of the Qinghai-Tibetan Plateau could be obtained through the analysis of the distribution and variation characteristics of microwave land surface emissivity of the region. At the same time, research based on land surface emissivity is helpful to improve the calculation of surface radiation budget and its influence on energy cycle in this region, and provide more abundant information for the systematic study of the influence of this region on weather and climate change.

2.3. Datasets

The components of atmospheric radiation and atmospheric transmittance in Equation (1) were calculated using the National Oceanic and Atmospheric Administration Community Radiative Transfer Model and the NCEP-FNL surface skin temperature, atmospheric temperature and humidity profiles.

2.3.1. Satellite Data

The satellite microwave observations used to retrieve the land surface emissivity were the level 1 bright temperature data from the MWRI onboard the FY-3B meteorological satellite.

The MWRI instrument and its calibration are described in the literature [32,33]. The calibrated and geolocated brightness temperatures are produced jointly by the National Satellite Meteorological Center of China Meteorological Administration and the Shanghai Institute of Space Communication Technology. Similar to the AMSR-E instrument, the MWRI observes objects using conical scanning with a 45° incident angle. The MWRI has five frequencies and 10 channels (10.65, 18.7, 23.8, 36.5 and 89 GHz), each of which is a dual-polarization (horizontal and vertical) channel. Each of the MWRI channels has different characteristics. The 10.65 GHz channels have a greater penetration of the atmosphere than the other channels and are used to obtain surface parameters such as the surface temperature and soil moisture content. The 18.7 and 36.5 GHz channels are used to measure the microwave radiation characteristics of ice and snow to obtain information such as snow cover, snow depth and snow water equivalent. The 23.8 GHz channels detect the absorption of water vapor, which, combined with the brightness temperature data from the other channels, can be used to provide information about the local water columnar amount. The 89 GHz channels are sensitive to the scattering of radiation signals by particles of precipitation and can be used to obtain information about precipitation at ground level. The field of view (FOV) size and the location of each frequency signals by particles

of precipitation and can be used to obtain information about The specific channel characteristics are shown in Table 1.

In this study, the Qinghai-Tibet Plateau was taken as the research area. To avoid the loss of surface vegetation coverage in winter, data collected in summer were selected for this study, and the surface coverage types of the Qinghai-Tibet Plateau are relatively comprehensive and complete, so that retrieving results can be better analyzed. Moreover, for vegetation types, generally in the peak growth period in summer, the emissivity is relatively stable, which can be used as the characteristic emissivity. Furthermore, snow cover can heavily impact the change in land cover emissivity, especially in winter.

Table 1. MWRI channel characteristics.

Center Frequency/GHz	Polarization	Band Width/MHz	Instantaneous FOV/km	NE Δ T/K	Calibration Error (K)
10.65	H/V	180	51 × 85	0.5	1.5
18.7	H/V	200	30 × 50	0.5	1.5
23.8	H/V	400	27 × 45	0.5	1.5
36.5	H/V	900	18 × 30	0.5	1.5
89.0	H/V	3000	9 × 15	0.8	2.0

2.3.2. NCEP-FNL Modeling Data

Due to the high altitude, severe weather, and tough environment, few in situ observations have been conducted in the Qinghai-Tibetan Plateau [34]. Therefore, reanalysis products, which include full space-time coverage, are widely used in atmospheric research of the plateau.

The surface skin temperature data of the NCEP GDAS/FNL 0.25 Degree Global Tropospheric Analysis and Forecast Grids [35] were used as the parameters in Equation (1). These NCEP-FNL operational global analysis and forecast data are on $0.25^\circ \times 0.25^\circ$ grids prepared operationally every six hours at 00:00, 06:00, 12:00 and 18:00 UTC. This product is available from the Global Data Assimilation System (GDAS), which continuously collects observational data from the Global Telecommunications System and other sources for many different analyses. The FNL datasets are made using the same model as in the Global Forecast System, but the FNL datasets are prepared about an hour after the Global Forecast System is initialized. The FNL datasets are delayed so that more observational data can be used. The Global Forecast System is run earlier in support of time-critical forecast needs and uses the FNL data from the previous six-hour cycle as part of its initialization.

The analyses are available on the surface at 26 fixed (and other) pressure levels from 1000 to 10 mbar in the surface boundary layer and at some sigma layers, the tropopause and a few other layers. The parameters include the surface pressure, sea-level pressure, geopotential height, temperature, sea surface temperature, soil values (e.g., soil moisture /water content, soil temperature), ice cover, relative humidity, u- and v-winds, vertical motion, vorticity and ozone concentrations.

However, since the NCEP /FNL data is a “product” obtained by fusing numerical prediction products and observation data through data assimilation methods, it must contain the systematic error introduced by the interaction of the uncertainty of the observation data, the numerical prediction mode error and the assimilation method error [36].

3. Data Processing

The satellite brightness temperature data need to be processed into $0.25^\circ \times 0.25^\circ$ grid data to match the data sources. The probability of precipitation particles in the field of view is high when the satellite observes the ground. There are a large number of different sizes of cloud droplets, raindrops and ice crystals in the cloud from which microwave radiation signals from the ground are scattered during upward transmission [37,38]. Although microwave radiation can penetrate clouds, rain and the atmosphere, it is attenuated during the transmission process, which reduces the amount of radiation reaching the satellite sensor [39–42]. If the attenuated observations were

used to calculate the parameters, the retrieving results for the surface emissivity would be directly affected by the satellite observation errors. To reduce the influence of cloud coverage on the precision of the retrieving calculation, it is necessary to discriminate the precipitation pixels in the field of view to improve the retrieval accuracy. In this study, a scattering index (SI) was used to exclude those pixels affected by atmospheric scattering. The SI adopted in this paper is given below [39,43]:

$$SI = 451.9 - 0.44 \cdot Tb_{19v} - 1.775 \cdot Tb_{23v} + 0.00575 \cdot Tb_{23v}^2 - Tb_{89v}, \quad (5)$$

where Tb is the brightness temperatures associated with MWRI channels. The global scattering index (SI) is developed by Grody for use with the SSM/I sensor [39]. Further refinement of the technique was described by Ferraro et al [44,45].

Through an exhaustive evaluation, Grody found that an SI value of 10 K or greater was a good global indicator of rain. A lower threshold does detect more rain at the cost of an increase in false alarms. In summary, the SI values greater than 10 K identify rain areas. Any measurement with the SI value of 8 K or greater is flagged as a rain-affected pixel. The SI index above has been calibrated with the ground-based radar measurements from the USA, Japan, and the United Kingdom [46]. Compared with the most widely used rain/no-rain screen methodologies [46,47], the SI used here was further refined based on AMSR data and more fit for AMSR-E measurements [43]. Yang and Weng used the SI as Equation (5) to exclude those AMSR-E pixels affected by atmospheric scattering [27].

The channel frequencies of the MWRI and AMSR-E instruments are similar, although the MWRI does not have the two 6.925 GHz channels. Thus, the precipitation pixels in this study were eliminated when the SI value was >10 K to avoid any effect on the accuracy of the retrieving calculation.

The physical properties of water bodies and land surfaces are very different, with very different radiation characteristics. Therefore, it is necessary to distinguish between these two types of surface before retrieving the land surface emissivity. In this study, the LandSeaMask dataset in the MWRI microwave data was used to distinguish between water bodies and land.

Figure 1 shows the vertical polarized brightness temperature with discrimination of the precipitation and water pixels over the Qinghai-Tibetan Plateau on 1–7 July 2017; the water pixels, such as Nam Lake and Selin Lake, have been removed. The vertical polarized brightness temperature over the Qinghai-Tibetan Plateau varies between 250 and 300 K. The brightness temperature is usually >270 K north of 32° N, whereas the values south of this latitude are generally between 250 and 260 K. The Himalaya lie from 26° to 28° N and have a brightness temperature <270 K.

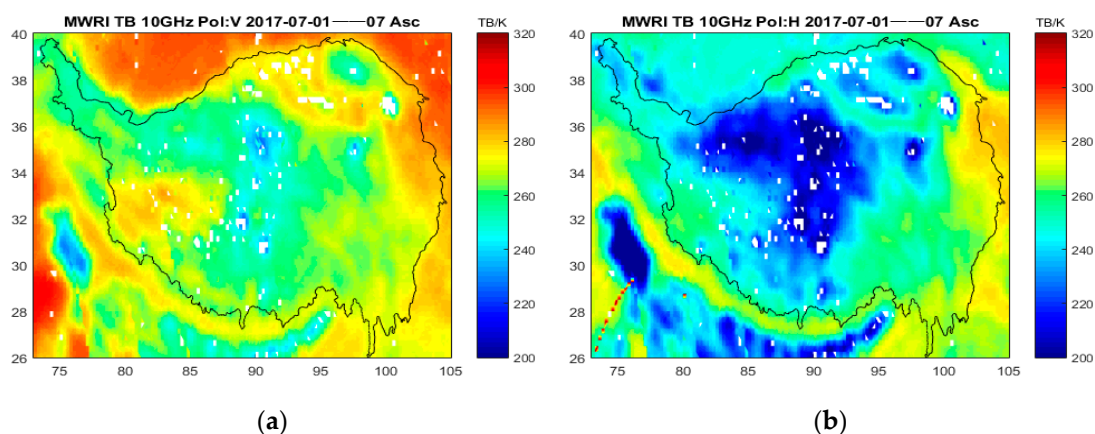


Figure 1. Microwave brightness temperature on 1–7 July 2017 (clear sky, land only, 10 GHz, vertical polarization): (a) vertical polarization; and (b) horizontal polarization.

The MWRI microwave EO data processed to a $0.25^\circ \times 0.25^\circ$ grid were spatially matched to the NCEP-FNL reanalysis data at the same resolution. The satellite passed over the study area at about 19:00–20:00 UTC. Because changes in surface skin temperature occur relatively slowly, the NCEP-FNL

surface skin temperature data from 18:00 UTC, which was closest to the time at which the satellite passed over the study region, were used to retrieve the land surface emissivity.

4. Results and Discussion

The instantaneous land surface emissivity when the satellite passed over the study region on 1–7 July 2017 were calculated from Equation (1). Figure 2 shows the land surface emissivity retrieving results at 10 GHz for vertical and horizontal polarization and the difference in polarization. The values of surface emissivity for vertical polarization were larger than those for horizontal polarization at the same frequency. Most of the values of surface emissivity at 10 GHz for vertical polarization over the Qinghai-Tibetan Plateau were >0.9 (Figure 2a) and the values of horizontal polarization were between 0.75 and 0.95 (Figure 2b). The vertical polarized surface emissivity was higher in the northwest and was usually >0.95 , whereas that in the southeast was between 0.87 and 0.92 (Figure 2a). The horizontal polarized surface emissivity was lower in the northwest, except at the edge of the plateau, and was between 0.75 and 0.85 in other areas (Figure 2b). The horizontal polarized surface emissivity in the southeast was relatively high (between 0.85 and 0.9). The difference in polarization of the surface emissivity was greatest in the northwest and gradually decreased from 0.15 in the northwest to nearly 0 in the southeast (Figure 2c).

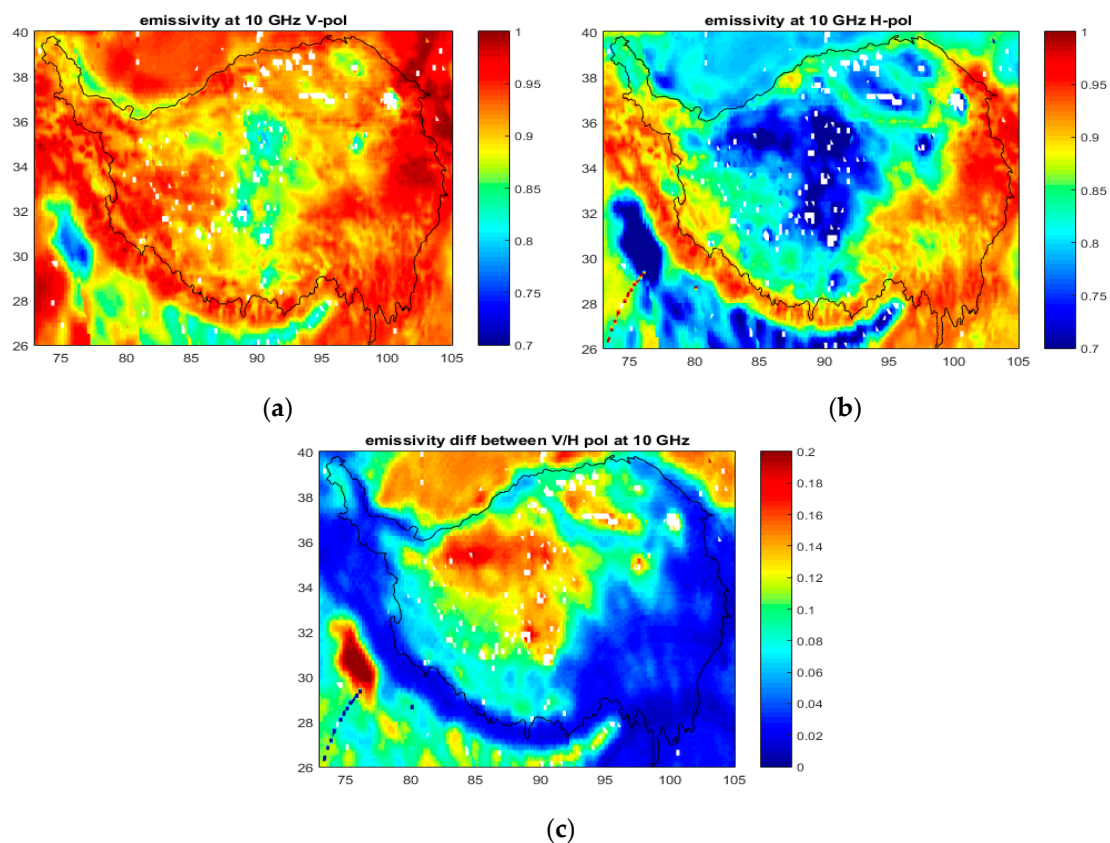


Figure 2. Land surface emissivity and differences between vertical and horizontal polarization at 10.65 GHz: (a) vertical polarization; (b) horizontal polarization; and (c) differences between the two polarizations.

The characteristics of surface emissivity in the study area were compared with the ground cover data. The surface coverage data used in this study were from the MWRI Landcover datasets, in which IGBP land surface coverage data at 89 GHz are stored with a horizontal resolution of $9 \text{ km} \times 15 \text{ km}$ (Figure 3). As the satellite passed over the study region on the scanning orbit, the surface coverage types from the northwest to the southeast of the Qinghai-Tibetan Plateau changed from bare

or semi-desert to grassland with trees, prairie, permanent wetlands, grassland with trees, deciduous broadleaved forest and evergreen broadleaved forest (Figure 3 and Table 2).

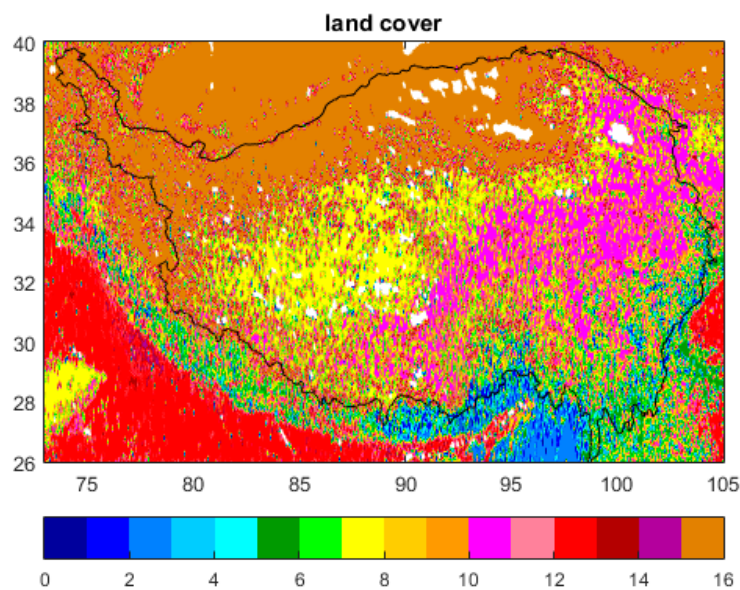


Figure 3. IGBP land cover classification map.

Table 2. Codes for land cover types included in the IGBP map.

Surface Coverage Type	Number	Surface Coverage Type	Number
Evergreen coniferous forest	1	Savanna	9
Evergreen broadleaved forest	2	Prairie	10
Deciduous coniferous forest	3	Permanent wetlands	11
Deciduous broadleaved forest	4	Crops	12
Mixed forest	5	City	13
Closed shrublands	6	Crops and natural vegetation	14
Sparse thickets	7	Snow and ice	15
Grassland with trees	8	Bare or semi-desert	16

The vertically and horizontally polarized land surface emissivity at 10 GHz and the difference in polarization were consistent with the spatial variation in the land surface cover type on the Qinghai-Tibetan Plateau. Norouzi et al. also found that emissivity values have frequency dependency over different land-cover types [48]. The northwest of the Qinghai-Tibetan Plateau is bare or semi-desert and the southeast is covered by shrubland, grassland, forest and other vegetation. The vertical polarized surface emissivity was higher in the northwest than in the southeast, whereas the horizontal polarized surface emissivity was lower in the northwest than in the southeast. The difference in polarization was much larger in the northwest than in the southeast. This is most likely because the type of vegetation coverage is closely related to the roughness of the surface. The smaller is the surface roughness, the closer it is to a mirror surface and the greater is the difference in the polarization of the surface emissivity. As the surface roughness increases, the scattering effect in each direction also increases, which leads to a gradual decrease in the difference in polarization until it becomes zero. There is almost no vegetation cover on the surface of deserts and therefore the surface is flat, the roughness is small and the difference in polarization of the surface emissivity is large. Land surfaces covered by vegetation, such as forests, in which there is a wide variety of sizes, types and locations of scattering surfaces and thus a high surface roughness, show a smaller difference in polarization. The result is in agreement with the conclusion obtained by Zhang et al. that the emissivity of vegetation including forests, grasslands and croplands is higher than that over bare soil, and the polarization difference of vegetation is smaller than that of bare soil [49]. Evaluation of roughness effects by the Hr parameter

(i.e., surface roughness) showed that some spatial patterns in the Hr values could be associated with the main vegetation types (higher values of Hr were retrieved generally in forested regions, intermediate values were obtained over crops and grasslands, and lower values were obtained over shrubs and desert) and topography [50].

Figure 4a–e shows the retrieving results for the surface emissivity obtained from the MWRI vertical polarization channels. In general, the surface emissivity increases with frequency, although it decreases with increasing frequency on part of the northern boundary of the Qinghai-Tibetan Plateau. This is because the northern part of the Qinghai-Tibetan Plateau is desert and the scattering effect increases with increasing frequency at a constant angle of incidence.

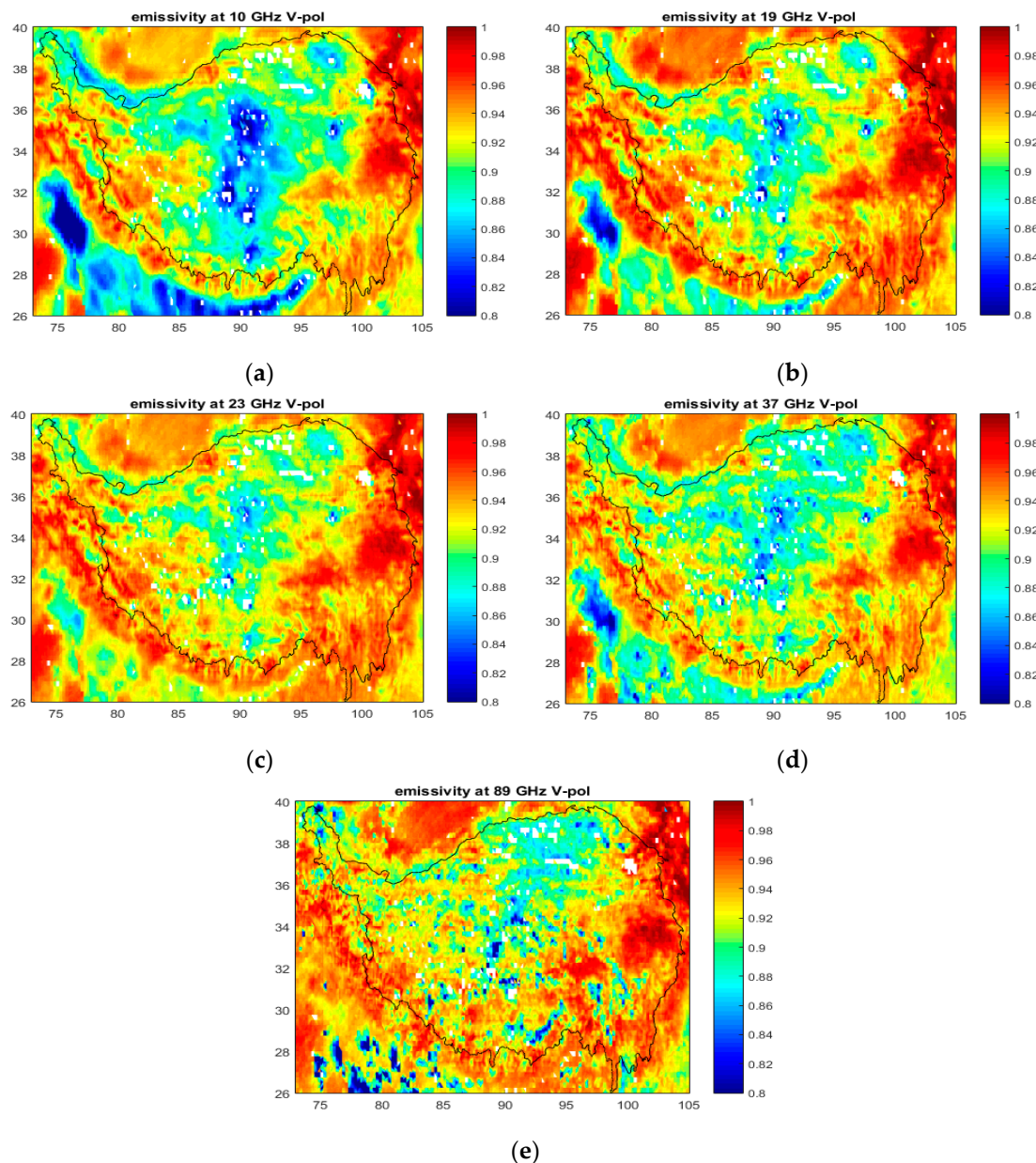


Figure 4. Land surface emissivity at 10, 19, 23, 36 and 89 GHz for vertical polarization: (a) 10 GHz; (b) 19 GHz; (c) 23 GHz; (d) 36 GHz; and (e) 89 GHz.

As mentioned above, surface emissivity is one of the decisive surface physical and biochemical parameters that determine the surface radiation budget. Therefore, the spatial and temporal evolution characteristics of surface emissivity of different surface cover types need to be quantitatively analyzed.

The factors affecting the change of surface emissivity also need to be understood. It is of vital importance to accurately describe the characteristics of land surface information, exchange energy between land surface and atmosphere, and drive global and regional climate models.

Figure 5a–p shows the variation trend of mean emissivity both at vertical and horizontal polarization with frequency of 16 different land surface types based on IGBP over the Qinghai-Tibetan Plateau on 1–7 July 2017. The horizontal axis is frequency and the vertical axis is emissivity. It can be seen that the emittance of V polarization is higher than that of H polarization, which conforms to physical laws. The microwave emissivity under different frequencies and polarities mainly varies with the type of land surface. The main influencing factors include: surface type, water content, surface roughness, surface skin temperature and atmospheric state. For different types of vegetation cover, the overall change trend of emissivity increases with the increase of frequency, while the polarization difference decreases with the increase of frequency. This is because with the increase of frequency, the scattering effect of vegetation body is enhanced and the radiation of vegetation is enhanced. As a result, the total radiation increases with the increase of frequency, and the polarization difference of body scattering is reduced. It should be noted that, at 18–23 GHz, the emissivity suddenly increases, which is inconsistent with the normal spectrum characteristics of the surface emissivity (generally a smooth curve) [26,51,52], possibly because 23.8 GHz is located near the water vapor absorption zone.

As summer is the vigorous season for plant growth, there is little difference in emissivity between evergreen coniferous forest and deciduous coniferous forest (Figure 5a,c), and between evergreen broad-leaved forest and deciduous broad-leaved forest (Figure 5b,d). For vegetation (evergreen/deciduous coniferous/broad-leaved forest, mixed forest, shrub, grassland, crop, etc.), the emissivity increased significantly from 10.65 to 23.8 GHz, and the polarization difference decreased significantly with the increase of frequency. The radiation characteristics such as vegetation absorption and attenuation mainly depend on the dielectric properties, density and size of vegetation components, such as the size of leaves and branches and the scale of relative wavelength. Therefore, the increase of vegetation density will increase the emissivity of H polarization and reduce the polarization difference [47]. Compared with shrub (Figure 5f,g), savanna (Figure 5i), prairie (Figure 5j), coniferous forest (Figure 5a,c), and broad-leaved forest (Figure 5b,d) have more dense vegetation and relatively small polarization difference. It can be seen in Figure 5j that the emissivity of prairie under H polarization is lower than that of forest cover. With the decrease of vegetation density, the contribution of bare soil in the pixel to the emissivity increases, reducing the emissivity of H polarization of the pixel [50]. V polarization emissivity is also relatively low compared with that of forests.

In urban areas (Figure 5m), H polarization has a higher emissivity than sparse thickets (Figure 5g), crops and natural vegetation (Figure 5n), and bare or semi-desert (Figure 5p). The emissivity of the V polarization is almost the same as that of the forest; However, the polarization difference was larger than that of forests and smaller than bare or semi-desert. This may be due to multiple scattering of city buildings. The emissivity of crops and natural vegetation (Figure 5n) is comprehensively affected by various land features, and the variation trend with frequency is similar to that of other vegetation types. For bare or semi-desert (Figure 5p), the emissivity of V polarization changes little, while that of H polarization increases with the increase of frequency, and the polarization difference is relatively large compared with that of vegetation. For the flat surface such as desert, the roughness is small, so overall the emissivity is lower.

In addition to the obvious spectral characteristics [53,54], the surface emissivity is closely related to the surface type and the surface state of the object, and with surface cover, surface roughness, soil moisture, soil texture, mineral composition, soil particle size, surface oxides on objects, surface impurities or coatings [2,55]. Different types of land cover are the result of a combination of these factors. The surface emissivity varies with the type of land cover and is closely related to the underlying vegetation and soil ratio [56].

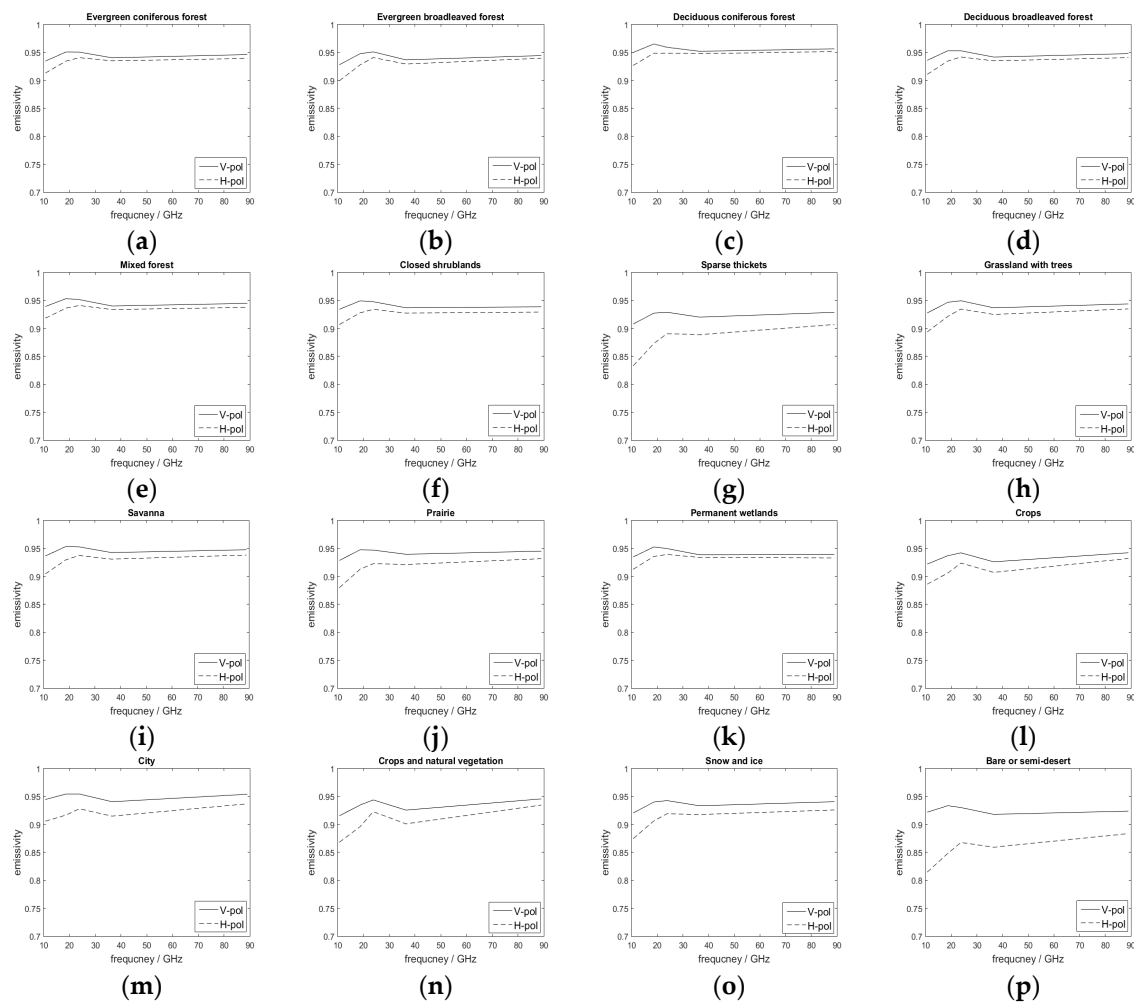


Figure 5. Land surface emissivity spectra: (a) evergreen coniferous forest; (b) evergreen broadleaved forest; (c) deciduous coniferous forest; (d) deciduous broadleaved forest; (e) mixed forest; (f) closed shrublands; (g) sparse thickets; (h) grassland with trees; (i) savanna; (j) prairie; (k) permanent wetlands; (l) crops; (m) city; (n) crops and natural vegetation; (o) snow and ice; and (p) bare or semi-desert.

As mentioned above, there are several factors that determine the accuracy of the retrieving results. Collocation has an influence on the accuracy of the retrieval results. In this study, the NCEP/FNL reanalysis dataset for the surface skin temperature, atmospheric temperature and humidity profiles was used. These data are only recorded four times per day at 00:00, 06:00, 12:00 and 18:00 UTC. Therefore, the surface skin temperature at the time closest to the time the satellite passed over was selected for retrieving. Although the surface skin temperature only changes slowly over short time periods, incomplete matching between the two data sources will have a large influence on calculations of the instantaneous surface emissivity. The error caused by this time mismatch is influenced by many factors and has a large uncertainty. Yang and Weng [27] found that a 1% error in the surface skin temperature would result in a 1% error in land emissivity. The error in the land surface temperature is a main source of error in emissivity at the frequencies less than 19 GHz [27]. The emissivity error from the errors in the atmosphere profile was also obtained. Moreover, the error in atmospheric profiles has more influence at higher frequencies where the emission-based radiative transfer could be more problematic. In addition, an error of 1% in T_b can result in an error of more than 1% in emissivity, depending upon upwelling and downwelling radiative components [27]. Therefore, further studies should be conducted towards assessing the effect of this error on the accuracy of surface emissivity retrieving results.

The existence of cloud liquid water, and ice particles in the atmosphere can significantly modify brightness temperatures, particularly at frequencies higher than 10 GHz [27,39]. To make the retrieval of surface emissivity from satellite measurements more accurate, the observations modified by atmospheric scattering due to large rain and ice particles need to be identified [27]. The precipitation pixel discrimination scheme applied to the SSM/I measurements was used directly on the FY-3B/MWRI data, ignoring any differences in applicability and the effects of the direct diversion scheme for distinguishing pixels on the retrieving results require further study. If the threshold for distinguishing pixels is set too small, then the number of pixels discriminated is low, which leads to a large percentage of the satellite brightness temperature measurements used in the retrieving process being affected by precipitation particles, which, in turn, affects the precision of the retrieving calculation for the surface emissivity. The precipitation particles have a strong attenuation effect on microwave radiation signals from the surface, and therefore the effect of setting too small a threshold is that the inaccuracy and the bias affecting the results becomes bigger. The available satellite brightness temperature data cannot be used when the threshold setting is too large. Therefore, it is important to set the correct threshold value for the optimum use of the satellite brightness temperature data when the precipitation pixels are discriminated. In this study, 10 K was used as the threshold in the precipitation pixel discrimination scheme, although further research is required to determine whether it is applicable to the MWRI data and the Qinghai-Tibetan Plateau.

5. Conclusions

The Qinghai-Tibetan Plateau plays an important role in climate change because of its unique characteristics. Among the surface parameters, surface emissivity is one of the most important surface parameters. Firstly, if the surface emissivity is known, the surface information can be separated from the brightness temperature of the satellite, so that the retrieval accuracy of atmospheric parameters can be improved. Secondly, surface emissivity can provide information on the changes of land surface and vegetation properties at regional scale or larger scale, so as to more accurately retrieve surface parameters.

In this study, the microwave land surface emissivity of the Qinghai-Tibetan Plateau was calculated under clear atmospheric conditions based on Level 1 brightness temperatures from the FY-3B/MWRI and the NCEP-FNL Global Operational Analysis dataset. The spectral characteristics and spatial distribution of the calculated emissivity data were subsequently analyzed according to the IGBP land cover classification dataset and the sources of calculated errors were considered.

The results show that the spatial distribution of the land surface emissivity was consistent with the type of land surface, showing a large difference in the polarization of surface emissivity in the northwest and a smaller difference in the southeast of the Qinghai-Tibetan Plateau. The effects of vegetation on the difference in polarization of the microwave emissivity was small in the southeast of the plateau, but was larger for the bare land and semi-deserts in the northwest. Diverse vegetation can be clearly seen in the retrieving results. The emissivity for almost all 16 types from IGBP at dual-polarization (vertical and horizontal) increases with the increase of frequency. In addition, the emissivity is closely related to the type of vegetation cover. The emissivity of the land surface covered by vegetation is higher than that of bare soil. Therefore, with the decrease of vegetation density, the contribution of bare soil increases, leading to the decrease of overall emissivity.

Finally, the source of retrieval error is analyzed. There are potential sources of error in the land surface emissivity calculations over the Qinghai-Tibetan Plateau.

First, in this study, the MWRI instantaneous brightness temperature observational data were matched in space with the surface skin temperature and atmosphere profiles from the NCEP-FNL reanalysis dataset, not in time, which would affect the final retrieval results. The fact that skin temperature changes slowly might not be enough to justify the choice of using the nearest neighbor point, which would lead to major biases in calculations. A temporal interpolation of reanalysis dataset should also be considered, in which different interpolation schemes should be evaluated.

Second, the same method used to discriminate precipitation pixels from SSM/I channels was used for the FY-3B/MWRI measurements, which may affect the quality control of the satellite data because the resulting errors would be transferred to the retrieving results of the surface emissivity.

Third, the quality of these auxiliary datasets, such as atmospheric temperature, water vapor, and surface skin temperature, directly affects the emissivity accuracy.

As future work, a database of surface emissivity for long-term sequences on the Qinghai-Tibetan Plateau should be established. In addition, it is necessary to quantify the errors caused by precipitation pixel discrimination scheme and spatial and temporal collocation of the auxiliary datasets; even standard procedures may need to be improved as well. Moreover, how to complete surface emissivity retrieval under cloudy or rainy conditions is the next research direction.

Author Contributions: Conceptualization: Y.W.; Methodology: Y.W. and B.Q.; Software: Y.W.; Validation: Y.W. and B.Q.; Formal analysis: Y.W., Y.B. and G.P.P.; Investigation: Y.W.; Resources: Y.B.; Data curation: X.L., L.L.; Writing—original draft preparation: Y.W.; Writing—review and editing: Y.W., Y.B. and G.P.P.; Visualization: Y.W.; Supervision: Y.B.; Project administration: Y.B.

Funding: This study was supported by the National Key Research and Development Program of China (2017YFC1501704, 2018YFC1407200, 2016YFA0600703), Jiangsu province basic research youth fund project of China (BK20150911), Pre-research project of SASTIND for the 13th Five-Year Plan (D010107), National Natural Science Foundation of China (41305033, 41675028) and Projects of Key Laboratory of Radiometric Calibration and Validation for Environmental Satellites, National Satellite Meteorological Center, China Meteorological Administration. G.P.P.'s participation was supported financially by the European Union's Horizon 2020 Marie Skłodowska-Curie Project "ENViSloN-EO" (grant agreement No 752094).

Acknowledgments: We thank the anonymous reviewers for the comments that helped improving our manuscript.

Conflicts of Interest: The authors declare no conflict of interest.

References

- Errico, R.M.; Ohring, G.; Weng, F.; Bauer, P.; Ferrier, B.; Mahfouf, J.F.; Turk, J. Assimilation of satellite cloud and precipitation observations in numerical weather prediction models. *J. Atmos. Sci.* **2007**, *64*, 3737–3741. [[CrossRef](#)]
- Yan, B.H.; Weng, F.Z. Effects of microwave desert surface emissivity on AMSU-A data assimilation. *IEEE Trans. Geosci. Remote Sens.* **2011**, *49*, 1263–1276. [[CrossRef](#)]
- Prigent, C.; Liang, P.; Tian, Y.; Aires, F.; Moncet, J.-L.; Boukabara, S.A. Evaluation of modeled microwave land surface emissivities with satellite-based estimates. *J. Geophys. Res. Atmos.* **2015**, *120*, 2706–2718. [[CrossRef](#)]
- Weng, F.Z.; Zhu, T.; Yan, B.H. Satellite data assimilation in numerical weather prediction models. Part II: Uses of rain affected microwave radiances for hurricane vortex analysis. *J. Atmos. Sci.* **2007**, *64*, 3910–3925. [[CrossRef](#)]
- He, W.Y.; Chen, H.B.; Xuan, Y.J.; Li, J.; Yin, J.H.; Xia, J.R.; Ji, Q.; Cai, X.Q. Field Measurements of the surface microwave emissivity for different surface types. *Prog. Geophys.* **2010**, *25*, 1983–1993. (In Chinese) [[CrossRef](#)]
- Moncet, J.-L.; Liang, P.; Galantowicz, J.F.; Lipton, A.E.; Uymin, G.; Prigent, C.; Grassotti, C. Land surface microwave emissivities derived from AMSR-E and MODIS measurements with advanced quality control. *J. Geophys. Res.* **2011**, *116*, D16104. [[CrossRef](#)]
- Furuzawa, F.A.; Masunaga, H.; Nakamura, K. Development of a land surface emissivity algorithm for use by microwave rain retrieval algorithms. In Proceedings of the Remote Sensing of the Atmosphere, Clouds, and Precipitation IV. International Society for Optics and Photonics, Honolulu, HI, USA, 24–26 September 2018.
- Grody, N.C. Severe storm observations using the Microwave Sounding Unit. *J. Appl. Meteorol.* **1983**, *22*, 609–625. [[CrossRef](#)]
- Jones, A.S.; Vonder Haar, T.H. Retrieval of surface emittance over land using coincident microwave and infrared satellite measurements. *J. Geophys. Res.* **1997**, *102*, 13609–13626. [[CrossRef](#)]
- Prigent, C.; Rossow, W.B.; Matthews, E. Microwave land surface emissivities estimated from SSM/I observations. *J. Geophys. Res.* **1997**, *102*, 21867–21890. [[CrossRef](#)]
- Prigent, C.; Wigneron, J.-P.; Rossow, W.B.; Pardo-Carrion, J.R. Frequency and angular variations of land surface microwave emissivities: Can we estimate SSM/T and AMSU emissivities from SSM/I emissivities? *IEEE Trans. Geosci. Remote Sens.* **2000**, *38*, 2373–2386. [[CrossRef](#)]

12. Prigent, C.; Aires, F.; Rosso, W.B. Land surface microwave emissivities over the globe for a decade. *Bull. Am. Meteorol. Soc.* **2006**, *87*, 1573–1584. [[CrossRef](#)]
13. Wilke, G.D.; Mcfarland, M.J. Correlations between Nimbus-7 Scanning Multichannel Microwave Radiometer data and an antecedent precipitation index. *J. Appl. Meteorol.* **1986**, *25*, 227–238. [[CrossRef](#)]
14. Galantowicz, J.F.; Moncet, J.-L.; Liang, P.; Lipton, A.E. Subsurface emission effects in AMSR-E measurements: Implications for land surface microwave emissivity retrieval. *J. Geophys. Res.* **2011**, *116*. [[CrossRef](#)]
15. Ringerud, S.; Kummerow, C.D.; Peters-Lidard, C.D. A Semi-Empirical Model for Computing Land Surface Emissivity in the Microwave Region. *IEEE Trans. Geosci. Remote Sens.* **2015**, *53*, 1935–1946. [[CrossRef](#)]
16. Qiu, Y.; Shi, J.; Hallikainen, M.; Lemmetyinen, J. The AMSR-E instantaneous emissivity estimation and its correlation, frequency dependency analysis over different land covers. In Proceedings of the IEEE International Geoscience and Remote Sensing Symposium (IGARSS), Boston, MA, USA, 8–11 July 2008; pp. 749–752.
17. Tian, Y.; Peters-Lidard, C.D.; Harrison, K.W.; Prigent, C. Quantifying uncertainties in land-surface microwave emissivity retrievals. *IEEE Trans. Geosci. Remote Sens.* **2012**, *52*, 829–840. [[CrossRef](#)]
18. Li, Z.L.; Wu, H.; Wang, N.; Qiu, S. Land surface emissivity retrieval from satellite data. *Int. J. Remote Sens.* **2013**, *34*, 3084–3127. [[CrossRef](#)]
19. Wang, Y.Q.; Shi, J.C.; Liu, Z.H.; Peng, Y.J.; Liu, W.J. Retrieval algorithm for microwave surface emissivities based on multi-source, remote-sensing data: An assessment on the Qinghai-Tibet Plateau. *Sci. China Earth Sci.* **2013**, *56*, 93–101. [[CrossRef](#)]
20. Gao, C.; Li, Z.L.; Qiu, S.; Tang, B.; Wu, H.; Jiang, X. An improved algorithm for retrieving land surface emissivity and temperature from MSG-2/SEVIRI data. *IEEE Trans. Geosci. Remote Sens.* **2014**, *52*, 3175–3191. [[CrossRef](#)]
21. Masiello, G.; Serio, C.; De Feis, I.; Amoroso, M. Kalman filter physical retrieval of surface emissivity and temperature from geostationary infrared radiances. *Atmos. Meas. Tech.* **2013**, *6*, 3613–3634. [[CrossRef](#)]
22. Masiello, G.; Serio, C.; Venafra, S.; Liuzzi, G. Kalman filter physical retrieval of surface emissivity and temperature from SEVIRI infrared channels: A validation and intercomparison study. *Atmos. Meas. Tech.* **2015**, *8*, 2981–2997. [[CrossRef](#)]
23. Tian, Y.; Peters-Lidard, C.D.; Harrison, K.W.; You, Y. An examination of methods for estimating land surface microwave emissivity. *J. Geophys. Res. Atmos.* **2015**, *120*, 11114–11128. [[CrossRef](#)]
24. Orimoloye, I.R.; Mazinyo, S.P.; Nel, W.; Kalumba, A.M. Spatiotemporal monitoring of land surface temperature and estimated radiation using remote sensing: Human health implications for East London, South Africa. *Environ. Earth Sci.* **2018**, *77*, 77. [[CrossRef](#)]
25. Qu, Y.; Zhu, Z.; Chai, L.; Liu, S.; Montzka, C.; Liu, J.; Yang, X.; Lu, Z.; Jin, R.; Li, X.; et al. Rebuilding a Microwave Soil Moisture Product Using Random Forest Adopting AMSR-E/AMSR2 Brightness Temperature and SMAP over the Qinghai-Tibet Plateau, China. *Remote Sens.* **2019**, *11*, 683. [[CrossRef](#)]
26. Weng, F.; Yan, B.; Grody, N.C. A microwave land emissivity model. *J. Geophys. Res.* **2001**, *106*, 20115–20123. [[CrossRef](#)]
27. Yang, H.; Weng, F.Z. Error sources in remote sensing of microwave land surface emissivity. *IEEE Trans. Geosci. Remote Sens.* **2011**, *49*, 3437–3442. [[CrossRef](#)]
28. Melesse, A.M.; Frank, A.; Nangia, V.; Hanson, J. Analysis of energy fluxes and land surface parameters in a grassland ecosystem: A remote sensing perspective. *Int. J. Remote Sens.* **2008**, *29*, 3325–3341. [[CrossRef](#)]
29. Abramowitz, G.; Pouyanné, L.; Ajami, H. On the information content of surface meteorology for downward atmospheric long-wave radiation synthesis. *Geophys. Res. Lett.* **2012**, *39*, L04808. [[CrossRef](#)]
30. French, A.N.; Schmutge, T.J.; Ritchie, J.C.; Hsu, A. Detecting land cover change at the Jornada Experimental Range, New Mexico with ASTER emissivities. *Remote Sens. Environ.* **2008**, *11*, 1730–1748. [[CrossRef](#)]
31. Edwards, J.M. Radiative processes in the stable boundary layer. Part I. Radiative aspects. *Bound.-Layer Meteorol.* **2009**, *131*, 105–126. [[CrossRef](#)]
32. Yang, H.; Weng, F.; Lv, L.; Lu, N.; Liu, G.; Bai, M.; Qian, Q.; He, J.; Xu, H. The FengYun-3 microwave radiation imager on-orbit verification. *IEEE Trans. Geosci. Remote Sens.* **2011**, *49*, 4552–4560. [[CrossRef](#)]
33. Yang, H.; Lv, L.; Xu, H.; He, J. Evaluation of FY3B-MWRI instrument on-orbit calibration accuracy. In Proceedings of the IEEE International Geoscience and Remote Sensing Symposium, Vancouver, BC, Canada, 24–29 July 2011.

34. Zhang, R.; Koike, T.; Xu, X.; Ma, Y. A China-Japan cooperative JICA atmospheric observing network over the Tibetan Plateau (JICA/Tibet project): An overview. *J. Meteorol. Soc. Jpn.* **2012**, *90*, 1–16. [[CrossRef](#)]
35. NCEP GDAS/FNL 0.25 Degree Global Tropospheric Analyses and Forecast Grids (ds083.3). Available online: <https://rda.ucar.edu/#lfd?nb=y&b=topic&v=Land%20Surface> (accessed on 12 January 2019).
36. Bengtsson, L.; Hodges, K.I.; Hagemann, S. Sensitivity of the ERA-40 reanalysis to the observing system: Determination of the global atmospheric circulation from reduced observations. *Tellus* **2004**, *56*, 456–471. [[CrossRef](#)]
37. Prabhakara, C.; Nucciarone, J.J.; Yoo, J.-M. Examination of ‘global atmospheric temperature monitoring with satellite microwave measurements’: 1) theoretical considerations. *Clim. Chang.* **1995**, *30*, 349–366. [[CrossRef](#)]
38. Savage, R.C. The Transfer of Thermal Microwaves through Hydrometeors. Ph.D. Thesis, University of Wisconsin-Madison, Madison, WI, USA, 1976.
39. Grody, N.C. Classification of snow cover and precipitation using the special sensor microwave imager. *J. Geophys. Res. Atmos.* **1991**, *96*, 7423–7435. [[CrossRef](#)]
40. Huang, C.; Duan, S.B.; Jiang, X.G.; Han, X.J.; Leng, P.; Gao, M.F.; Li, Z.L. A physically based algorithm for retrieving land surface temperature under cloudy conditions from AMSR2 passive microwave measurements. *Int. J. Remote Sens.* **2019**, *40*, 1828–1843. [[CrossRef](#)]
41. Zhou, F.C.; Li, Z.L.; Wu, H.; Duan, S.B. A remote sensing method for retrieving land surface emissivity and temperature in cloudy areas: A case study over South China. *Int. J. Remote Sens.* **2019**, *40*, 1724–1735. [[CrossRef](#)]
42. Favrichon, S.; Prigent, C.; Jimenez, C.; Aires, F. Detecting cloud contamination in passive microwave satellite measurements over land. *Atmos. Meas. Tech.* **2019**, *12*, 1531–1543. [[CrossRef](#)]
43. Wilheit, T.; Kummerow, C.D.; Ferraro, R. Rainfall algorithms for AMSR-E. *IEEE Trans. Geosci. Remote Sens.* **2003**, *41*, 204–214. [[CrossRef](#)]
44. Ferraro, R.R.; Grody, N.C.; Marks, G.F. Effects of surface conditions on rain identification using the SSM/I. *Remote Sens. Rev.* **1994**, *11*, 195–209. [[CrossRef](#)]
45. Ferraro, R.R.; Smith, E.A.; Berg, W.; Huffman, G. A review of screening techniques for passive microwave precipitation retrieval algorithms. *J. Atmos. Sci.* **1998**, *55*, 1583–1600. [[CrossRef](#)]
46. Ferraro, R.R.; Marks, G.F. The development of SSM/I rain rate retrieval algorithms using ground-based radar measurements. *J. Atmos. Ocean. Technol.* **1995**, *12*, 755–770. [[CrossRef](#)]
47. Adler, R.F.; Huffman, G.J.; Keehn, P.R. Global tropical rain estimates from microwave adjusted geosynchronous IR data. *Remote Sens. Rev.* **1994**, *11*, 125–152. [[CrossRef](#)]
48. Norouzi, H.; Temimi, M.; Prigent, C.; Turk, J. Assessment of the consistency among global microwave land surface emissivity products. *Atmos. Meas. Tech.* **2015**, *8*, 1197–1205. [[CrossRef](#)]
49. Zhang, Y.P.; Jiang, L.M.; Qiu, Y.B.; Wu, S. Study of the microwave emissivity characteristics over different land cover types. *Spectrosc. Spectr. Anal.* **2010**, *30*, 1446–1451. [[CrossRef](#)]
50. Wang, S.; Wigneron, J.-P.; Jiang, L.M.; Parrens, M. Global-scale evaluation of roughness effects on C-Band AMSR-E observations. *Remote Sens.* **2015**, *7*, 5734–5757. [[CrossRef](#)]
51. Ulaby, F.T.; Moore, R.K.; Fung, A.K. *Microwave Remote Sensing: Active and Passive*; Artech House: Norwood, MA, USA, 1986; Volume II.
52. Ferrazzoli, P.; Guerriero, L. Passive microwave remote sensing of forests: A model investigation. *IEEE Trans. Geosci. Remote Sens.* **1996**, *34*, 433–443. [[CrossRef](#)]
53. Prigent, C.; Aires, F.; Rossow, W.; Matthews, E. Joint characterization of vegetation by satellite observations from visible to microwave wavelengths: A sensitivity analysis. *J. Geophys. Res.* **2001**, *106*, 20665–20685. [[CrossRef](#)]
54. Nerry, F.; Labeled, J.; Stoll, M.P. Spectral properties of land surfaces in the thermal infrared: 1. Laboratory measurements of absolute spectral emissivity signatures. *J. Geophys. Res.* **1990**, *95*, 7027–7044. [[CrossRef](#)]

55. Van de Griend, A.A.; Owe, M.; Groen, M.; Stoll, M.P. Measurement and spatial variation of thermal infrared surface emissivity in a savanna environment. *Water Resour. Res.* **1991**, *27*, 371–379. [[CrossRef](#)]
56. Pinker, R.T.; Sun, D.L.; Hung, M.P.; Li, C. Evaluation of satellite estimates of land surface temperature from goes over the United States. *J. Appl. Meteorol. Climatol.* **2009**, *48*, 167–180. [[CrossRef](#)]



© 2019 by the authors. Licensee MDPI, Basel, Switzerland. This article is an open access article distributed under the terms and conditions of the Creative Commons Attribution (CC BY) license (<http://creativecommons.org/licenses/by/4.0/>).